remote sensing

MDPI

Article

A New Approach to Identify On-Ground Lamp Types from Night-Time ISS Images

Natalia Rybnikova [1,2,3,*], Alejandro Sánchez de Miguel [4,5], Sviatoslav Rybnikov [6,7] and Anna Brook [8]

1 Department of Mathematics, University of Leicester, Leicester LE1 7RH, UK
2 Department of Natural Resources and Environmental Management, University of Haifa, Haifa 3498838, Israel
3 Department of Geography and Environmental Studies, University of Haifa, Haifa 3498838, Israel
4 Environment and Sustainability Institute, University of Exeter, Penryn Campus, Penryn TR10 9FE, UK; alejasan@ucm.es
5 Department Física de la Tierra y Astrofísica, Instituto de Física de Partículas y del COSMOS (IPARCOS), Universidad Complutense de Madrid, 28040 Madrid, Spain
6 Institute of Evolution, University of Haifa, Haifa 3498838, Israel; srybniko@campus.haifa.ac.il
7 Department of Evolutionary and Environmental Biology, University of Haifa, Haifa 3498838, Israel
8 Center for Spatial Analysis Research (UHCSISR), Spectroscopy & Remote Sensing Laboratory, Department of Geography and Environmental Studies, University of Haifa, Haifa 3498838, Israel; abrook@geo.haifa.ac.il
* Correspondence: nrybhiko@campus.haifa.ac.il; Tel.: +972-54-551-4755

Abstract: Artificial night-time light (NTL), emitted by various on-ground human activities, has become intensive in many regions worldwide. Its adverse effects on human and ecosystem health crucially depend on the light spectrum, making the remote discrimination between different lamp types a highly important task. However, such studies remain extremely limited, and none of them exploit freely available satellite imagery. In the present analysis, the possibility to remotely assess the relative contribution of different lamp types into outdoor lighting is tested. For this sake, we match two data sources: (i) the radiometrically calibrated RGB image provided by the ISS (coarse spectral resolution data), and (ii) a set of in situ measurements with detailed spectral signatures conducted by ourselves (fine spectral resolution data). First, we analyze the fine spectral resolution data: using spectral signatures of standard lamp types from the LICA UCM library as endmembers, we perform an unmixing analysis upon NTL in situ measurements; by this, we obtain the estimates for relative contributions of the standard lamp types in each examined in situ measurement. Afterward, we focus on the coarse spectral resolution data: by using various types of statistical models, we predict the estimated relative contributions of each lamp type via RGB characteristics of spatially corresponding pixels of the ISS image. The built models predict sufficiently well (with R^2 reaching ~0.87) the contributions of two standard lamp types: high-pressure sodium (HPS) and metal-halide (MH) lamps, the most widespread lamp types in the study area (Haifa, Israel). The restored map for HPS allocation demonstrates high concordance with the network of municipal roads, while that for MH shows notable coincidence with the industrial facilities and the airport.

Keywords: RGB; ISS; radiometric calibration; in situ measurement; lamp types; fine and coarse spectral signature; unmixing; statistical models

check for updates

Citation: Rybnikova, N.; Sánchez de Miguel, A.; Rybnikov, S.; Brook, A. A New Approach to Identify On-Ground Lamp Types from Night-Time ISS Images. *Remote Sens.* **2021**, *13*, 4413. https://doi.org/10.3390/rs13214413

Academic Editors: Lin Li, Mengjun Kang and Min Weng

Received: 30 September 2021
Accepted: 30 October 2021
Published: 2 November 2021

Publisher's Note: MDPI stays neutral with regard to jurisdictional claims in published maps and institutional affiliations.

Copyright: © 2021 by the authors. Licensee MDPI, Basel, Switzerland. This article is an open access article distributed under the terms and conditions of the Creative Commons Attribution (CC BY) license (https://creativecommons.org/licenses/by/4.0/).

1. Introduction

Artificial night-time light (NTL), emitted by various on-ground human activities, becomes further intensive in many countries, making the world brighter [1–3]. At that, there exist vast inequalities in the spatial distribution of NTL intensities: Thus, night light flux per capita in the USA on average is three times more than in Europe; across US counties, there exists a 16,000-fold difference between the most and the least light-polluted ones [4]. On the global scale, the most polluted countries (in terms of the populations living under polluted skies) are Saudi Arabia, South Korea, Argentina, Canada, Spain, the US, Brazil, Russia, Japan, and Italy [3]. Dynamics of NTL levels might be used for

monitoring globalization and urbanization processes, in addition to previously used GDP, CO^2 emissions, and total and urban population data [5].

At the same time, a huge amount of empirical evidence has been accumulated for the adverse effects of NTL on both humans [6–9] and ecosystems [10–13]. An especially serious concern is the long-term cumulative effects of NTL, which remain almost unexplored [14]. Moreover, NTL also frustrates professional astronomical observations [15–17]. With respect to the above-mentioned challenges, the necessity to regulate light pollution becomes furthermore recognized [18–20]. The adverse effects of NTL are known to depend crucially on the light spectrum [21,22]. For instance, the short-wavelength light stronger suppresses melatonin production and distorts circadian rhythms in mammals [9,23,24], while the long-wavelength light more strongly disrupts the magnetic orientation of migratory birds [25]. To date, the detailed spectral signatures are available for the majority of common lighting sources (see, for example, the LICA-UCM database [26]). Discriminating between different lamp types based on satellite imagery would allow for a more fine-tuned analysis of adverse health effects associated with NTL. In turn, this would contribute to elaborating more precise policies for diminishing light pollution.

In the meantime, studies aiming to discriminate between different lamp types remain extremely limited. In two of them, the authors tested the principal possibility to identify lamp type, proceeding from corresponding spectral signature, either detailed or aggregated. In the first study, Elvidge with co-authors analyzed spectral signatures of 43 different lamps representing nine the most widespread lamp types, using ASD spectroradiometer, implying measuring the signatures from 400 to 2500 nm with 10 nm bandwidth [27]. They showed that discriminant analysis correctly classified all lamp types when based on their detailed spectra. The authors also succeeded to find a minimum set of broad bands ensuring sufficient classification quality: under blue, green, red, and NIR bands (a slightly modified set represented on the Landsat Thematic Mapper), only 4.7% of the lamp types were classified incorrectly. In the second study by Sánchez de Miguel and co-authors, it was demonstrated that main lamp types can often be separated using color–color diagrams with G/R and B/G ratios as the two coordinates [28]. Accordingly, the RGB bands corresponded to Nikon D3s camera sensors, used by astronauts in the ISS. However, in both mentioned studies, the proposed lamp-type discriminating methods, although being based on spectral bands of existing satellites, were not tested on real imagery [27,28].

Puschnig with co-authors reported on spectroscopic observations of night sky spectra over Vienna, which were performed from the North Dome of the Vienna University Observatory [29]. The authors used an 80 cm Cassegrain telescope, a DSS-7 spectrograph, and a ST-7 CCD camera with a wavelength coverage of ~450–850 nm. As revealed, the strongest spectral line was due to the most common type of residential lighting type (i.e., a fluorescent lamp) and was located at 546 nm; the second-strongest line at 611 nm was revealed as a composition of fluorescent and high-pressure sodium lamps, used to illuminate main streets.

To the best of our knowledge, the only explicit test of such a kind was performed by Hale with co-authors for Birmingham, UK [30]. The authors analyzed a one-meter aerial image of the city and a layer reporting location and type of lamp. They succeeded in classifying four main lamp types with high accuracy (7.5% error), based on three focal statistics: B and G/R ratio for pixels up to 1 m from the lamp center and the maximum averaged RGB level for pixels between 2 and 4 m from the lamp center. At that, RGB bands corresponded to those of the Nikon D2X digital camera. This study, however, benefits from high-resolution aerial images available only for limited sites and are typically costly.

In the present study, we test for the possibility to identify on-ground lamp types from freely available satellite imagery of relatively coarse spatial and spectral resolution. For the study area of Haifa, Israel, we match two NTL data sources: (i) the radiometrically calibrated RGB image provided by the ISS (coarse spectral resolution data), and (ii) a set of in situ measurements with detailed spectral signatures conducted by ourselves (fine spectral resolution data). Since the ISS image is of ~20-m spatial resolution, each pixel may

represent a *mixture of lamps*. Thus, as the first step, we analyzed fine spectral resolution data: in situ measurements were subjected to unmixing analysis, with spectral signatures of the standard lamp types (from the freely available LICA UCM library [26]) used as endmembers. The unmixing analysis allowed us to estimate the relative contribution of different lamp types in each examined in situ measurement. Afterward, we switched to the analysis of the coarse resolution data: using various types of statistical models, we predicted the estimated relative contributions of each lamp type via RGB characteristics of spatially corresponding pixels of the ISS image. Finally, we applied the built models to restore the maps of the relative contribution of certain lamp types into outdoor lighting in the study area.

2. Materials and Methods

The study design comprises four main stages: (i) matching ISS RGB image with the in situ measurements—to select the representative ground truth observations; (ii) unmixing upon detailed spectral signatures of the selected representative in situ observations—to estimate the relative contributions of the standard lamp types; (iii) building statistical models—to predict the relative contributions via RGB characteristics of the corresponding pixels from the ISS image; and (iv) applying the models to all the pixels from the ISS RGB image—to restore the allocation of major lamp types in the study area. The methodological scheme of the study is reported in Figure 1 and described in detail in subsections below.

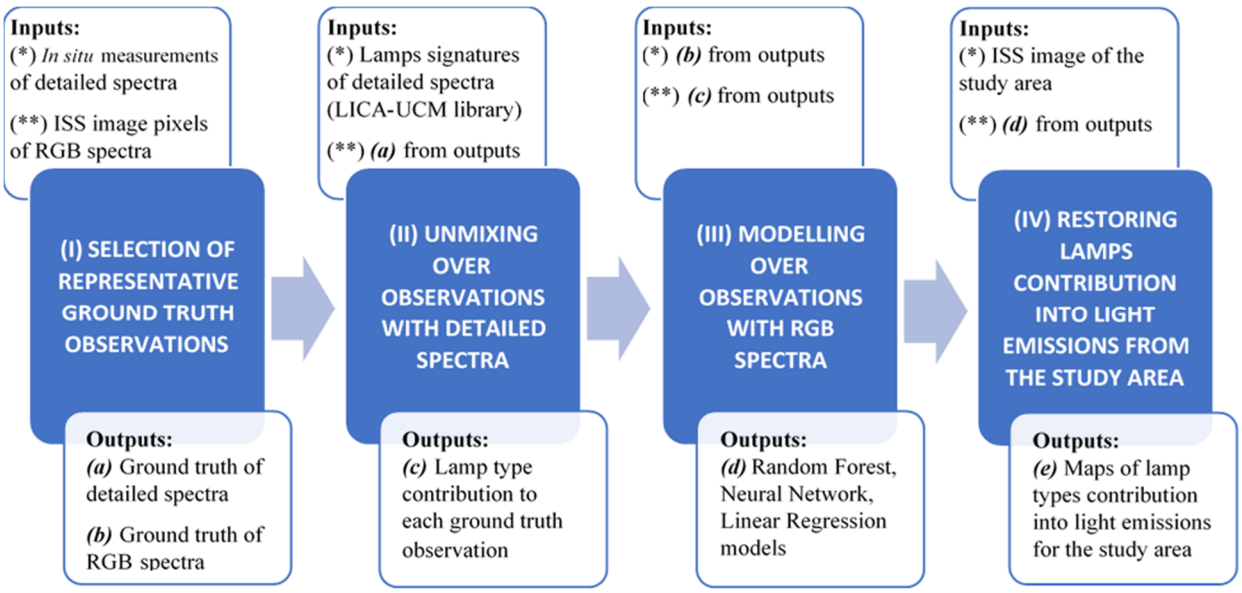


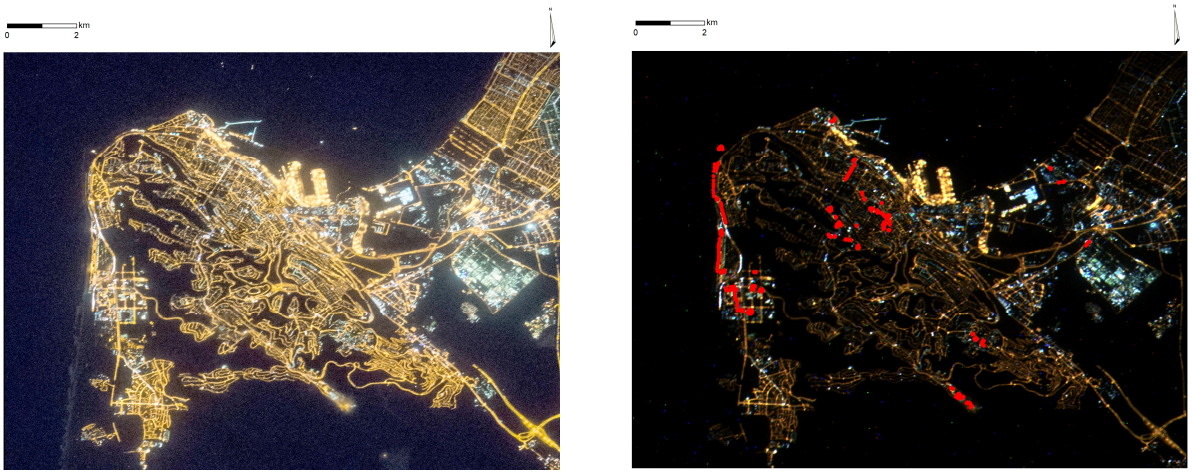
Figure 1. Methodological scheme of the study.

2.1. Data Sources

In the present analysis, two NTL data sources were used: (i) the radiometrically calibrated RGB image provided by the ISS (coarse spectral resolution data), and (ii) a set of in situ measurements with detailed spectral signatures conducted by ourselves (fine spectral resolution data).

The ISS-produced NTL image of Haifa (ISS045-E-148262) was taken on 29 November 2015, with the Nikon D4 DSLR camera [31]. The image was georeferenced and radiometrically calibrated by SAVESTARS Consulting SL [32] according to the procedure reported in [33].

In situ NTL measurements were performed in March 2015 with the Konica Minolta CL-500A spectrometer. Each of the 610 measurements reports spectral irradiance (w/m^2) at a 1-nm pitch from 360 to 780 nm [34]. Figure 2 reports the original and the radiometrically calibrated RGB images from the ISS, overlaid with the in situ measurements localities.



(**a**) (**b**)

Figure 2. Georeferenced ISS-produced (taken on 29.11.2015 by Nikon D4 DSLR camera; ID ISS045-E-148262) (**a**) and radiometrically calibrated (**b**) night-time image of the Haifa region. In situ measurements (n = 610), performed in March 2015 via Konica Minolta CL-500A spectrometer, are marked by red dots in the right sub-figure.

Additionally, for unmixing analysis, we used spectral signatures of standard lamp types, taken from the freely available LICA UCM library [26]. We examined spectral signatures of 81 lamps representing seven (out of nine reported by Elvidge et al. [27]) of the most popular lamp types: fluorescent (FL), metal-halide (MH), high-pressure sodium (HPS), low-pressure sodium (LPS), incandescent and halogen (I&H), mercury-vapor (MV), and light-emitting diodes (LED). Two other widespread lighting types—liquid-fuel, and pressurized-fuel lamps—were omitted due to data unavailability.

2.2. Selection of the Representative Ground Truth Observations

Proceeding from the available data on the relatively coarse spatial resolution of ISS image, with each pixel reporting emissions from multiple light sources, and simultaneously given the sporadic point-wise available in situ NTL measurements, we selected among 610 observations only those which *in some sense* coincided with corresponding pixels in the ISS image. Since each pixel might be characterized by RGB radiances only, we first simulated the radiances of synthetic RGB bands of in situ measurements as if they would appear on the ISS sensors of Nikon D4 DSLR camera and then chose the observations with similar to the corresponding ISS imagery pixel (in terms of Euclidian distance in the coordinate system, represented by B/G and G/R ratios) RGB characteristics.

To simulate the radiance R (of either red, green, or blue band), we used the augmented equation reported by Sanchez de Miguel et al. [28]:

$$R = \frac{\int_0^\infty \phi(\lambda)T(\lambda)A(\lambda)d\lambda}{\int_0^\infty \phi_{AB}(\lambda)T(\lambda)A(\lambda)d\lambda}, \quad (1)$$

where

$\phi(\lambda)$ = spectrum of the lamp under analysis;
$T(\lambda)$ = spectral sensitivity of the synthetic band (in the present analysis, we used spectral responses of Nikon D4 Electronic Still Camera—the one that produced the image under analysis,—reported in [28])—see Figure 3a;
$A(\lambda)$ = atmospheric transmittance (in the present analysis, we applied the MODTRAN® computer code [35] for the simulation of atmospheric transmittance of light emissions through the atmosphere over the study area at the time when in situ measurements were performed. MODTRAN code addresses the following issues: the effects of molecular and particulate absorption/emission and scattering, surface reflections and emission, solar/lunar illumination, and spherical refraction [35])—see Figure 3b;

$\phi_{AB}(\lambda)$ = reference spectrum of AB magnitude system, defined for a source of constant spectral density flux of 3631 Janskys across the spectral range of the band [28]—see Figure 3c.

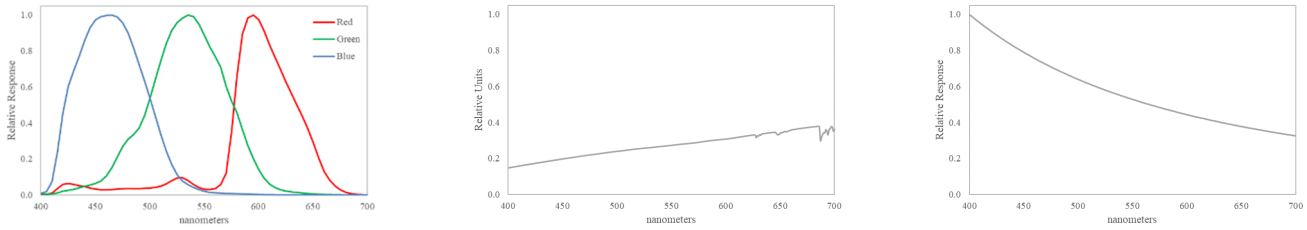


Figure 3. Graphical illustration of the constituents for synthetic bands' radiance computation: spectral sensitivity of RGB bands of Nikon D4 DSLR camera (**a**), atmospheric transmittance (**b**), and reference spectrum of AB magnitude system (**c**).

As a measure of similarity between RGB radiances, reported by pixels of calibrated ISS image, and corresponding in situ measurements, we used Euclidian distance in the coordinate system, represented by B/G and G/R ratios. Given the variance of such a distance ($d_{\max}$ = 2.00), we settled the threshold of $d < 0.2$.

2.3. Estimation of the Relative Contributions of the Standard Lamp Types into Spectral Signatures of the in Situ Observations

The detailed spectral signatures of the representative in situ measurements (see Section 2.2) were subjected to unmixing analysis. As the endmembers (i.e., spectra of pure 'materials'—see [36]), we used the detailed spectral signatures of the standard lamps from the LICA-UCM library. The end-members' signatures are shown in Figure 4. For unmixing analysis, we used the FNNLS algorithm [37], implemented in MATLAB v.R2020b. The algorithm returned the percentages of all endmember lamps in each of the pre-selected in situ measurements. The obtained percentages were then aggregated within lamp types, and the sums were normalized to the unit. The obtained estimates are hereafter referred to as relative contributions.

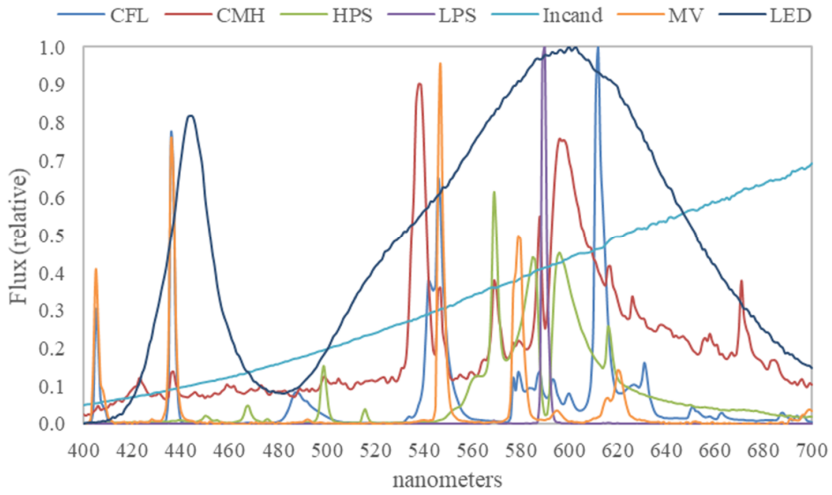


Figure 4. Spectral signatures of selected representatives of each lamp type used in the analysis. *Note*: The following lamps' signatures are depicted: 'CFL' = Compact Fluorescent Lamp of 2776K; 'CMH' = Ceramic Metal Halide of 2829K; 'HPS' = High-Pressure Sodium of 2005K; 'LPS' = Low Pressure Sodium of 1701K; 'Incand' = Incandescent Tungsten of 2805K; 'MV' = Mercury Vapor of 4717K; and 'LED' = LED of 3033K. At that, for lamp types under analysis, the temperatures varied in the diapason of 2478–5576K for 'CFL'; 2378–6075K for 'MH'; 1732–2176K for 'HPS'; 2021–2911K for 'Incand'; 4075–4741K for 'MV'; and 1833–9089K for 'LED'.

2.4. Prediction of the Relative Contributions via RGB Characteristics of the Corresponding Pixels from the ISS Image

The relative contribution of each lamp type, obtained in the unmixing analysis (Section 2.2), served as the dependent variable in a set of statistical models. As the explanatory variables, we tried different characteristics of the pixels of the calibrated ISS image: (i) radiance in the red, green, and blue bands per se; (ii) their ratios (G/R and B/G, or GG/RB ratio), and an additional derivative characteristic describing the pixel's 'proximity' to the lamp type in question. This distance was included in the models since we found that different lamps within each of the lamp types tend to lie along straight lines in the G/R, B/G coordinate plane (see Figure 5). We tried several formalizations of such a distance: (i) the ratio between B/G and G/R of the pixel, as a measure of the line's slope; (ii) Euclidean distance from the pixel to the line representing the lamp type in question; and (iii) Mahalanobis distance from the pixel to the cloud representing the lamp type in question, which accounts for both the center of mass and the direction of the cloud [38].

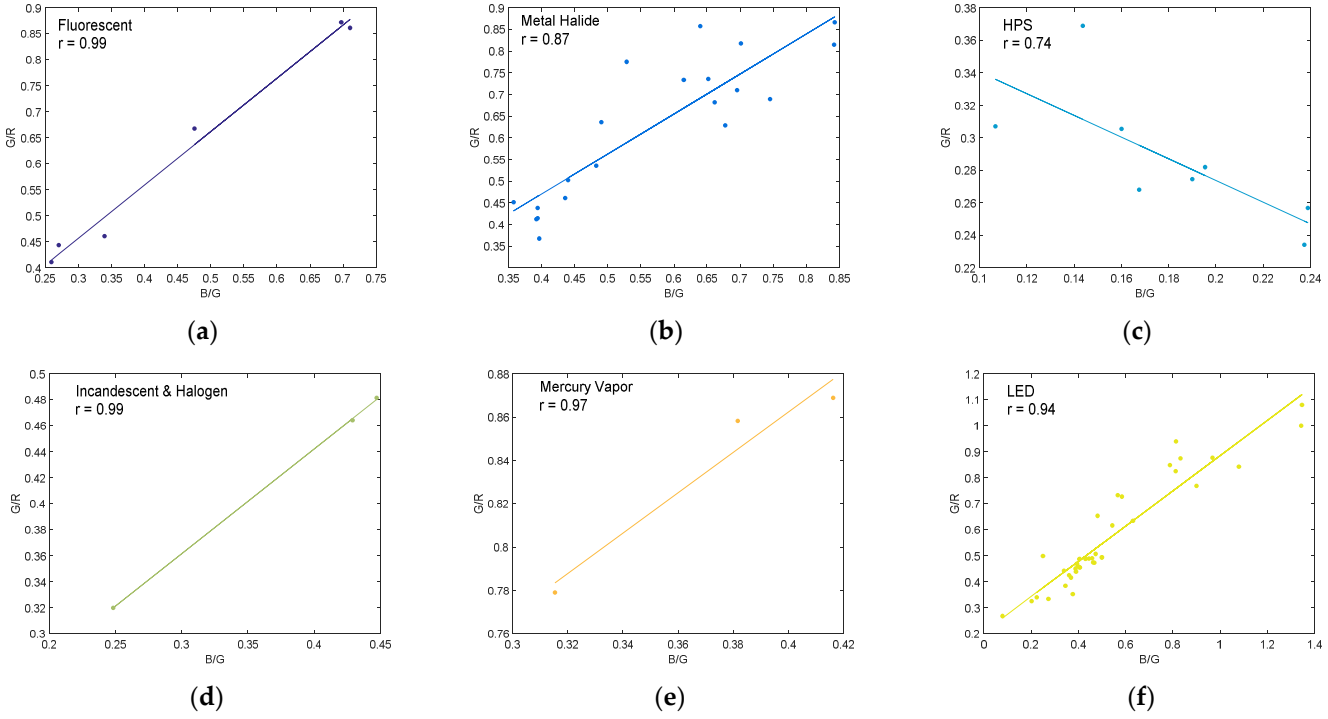


Figure 5. B/G vs. G/R ratios of the simulated synthetic bands: Fluorescent (**a**), Metal Halide (**b**), HPS (**c**), Incandescent (**d**), Mercury Vapor (**e**), and LED (**f**) lamps. *Note*: LPS lamp, reporting G/R = 0.18 and B/G = 0.02, is the only representative of the type and is not depicted in the figure.

We examined statistical models of several classes: multiple least-square linear regression, neural network (perceptron), and random forest. The general idea behind the multiple least-squares linear regression is fitting the observations (each represented by a point in N-dimensional space with (N-1) number of predictors and one dependent variable) by a linear relationship, represented by an (N-1)-dimensional linear surface, or hyperplane, by minimizing the sum of squared errors between the actual and estimated over this hyperplane levels of the dependent variable. In addition to the linear approach, a multi-layer neural network (perceptron)—a hierarchical model consisting of input, output, and several hidden layers of neurons, weighting, and summarizing the inputs from the previous layer and passing them to the neurons of the next layer—was treated. We also tested the random forest approach [39], which implies building an ensemble of decision trees, each 'voting' for a certain class or level of the dependent variable, with subsequent averaging of the estimates across all the decision trees.

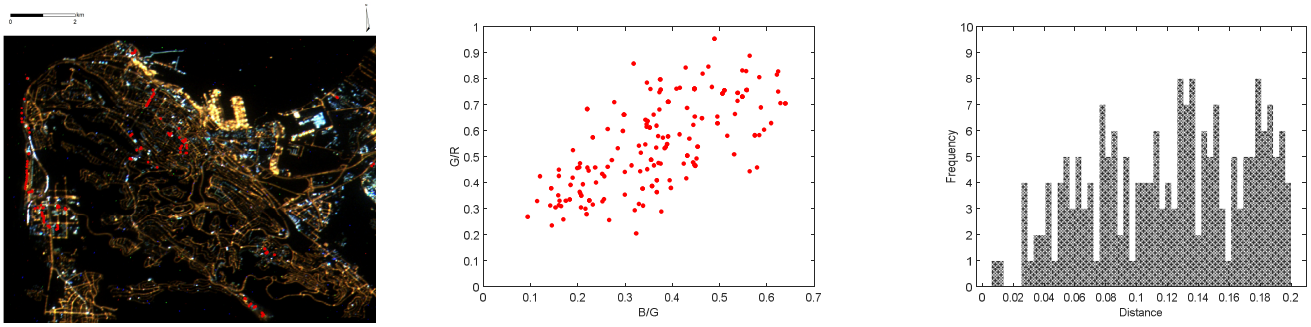
All models were run in ORANGE v.3.28 with the default settings. Specifically, *linear regression* was applied with intercept and without regularization. Like a *neural network*, we used a multi-layer perceptron with backpropagation; the model parameters were the following: number of neurons in the hidden layer is 100, number of hidden layers is 1, the activation function is ReLu, solver for weight optimization is a stochastic gradient-based optimizer, L2 penalty parameter is 0.0001, and the maximal number of iterations is 200. In *random forest* models, the number of trees was settled to 10, an arbitrary set of attributes and limit depth of individual trees were left unchecked, and subsets smaller than 5 were required not to be split. We conducted a five-fold cross-validation procedure, which implies: (i) splitting the data into five nearly equal subsets, (ii) using each of them as the testing set while using the other four as a training set, and (iii) averaging the performance scores from these five iterations separately across training and testing sets. The input database used in the analysis is available from the authors upon request.

2.5. Restoring the Allocation of Major Lamp Types in the Haifa Area (Israel)

Finally, the best-performing models (Section 2.4) were applied to the radiometrically calibrated ISS image (see Section 2.1), and estimates for different lamp type relative contribution into light emissions from the study area were obtained and depicted.

3. Results

Among all initially available in situ measurements, we chose only the set of *representative* measurements—those deviating from the corresponding pixels of the radiometrically calibrated ISS image by less than 0.2 in terms of the Euclidian distance in the G/R, B/G coordinate plane (see Section 2.2). Overall, we obtained 196 measurements; their main characteristics are reported in Figure 6.



(**a**) (**b**) (**c**)

Figure 6. Main characteristics of selected representative ground truth measurements: localities (marked as red dots) (**a**), G/R and B/G ratios (**b**), and Euclidian distances distribution from the corresponding ISS pixel in G/R, B/G coordinate system (**c**).

The detailed spectral signatures of the obtained 196 representative in situ measurements were then subjected to *unmixing analysis* (see Section 2.2). The results of the unmixing, i.e., the relative contributions of the seven endmember lamp types, are reported in Appendix A Table A1. In the table, we also report, for each in situ measurement, the highest correlation between its detailed spectral signature and the signatures of the lamps from the LICA-UCM library. As one can see from the table, the measurements with the predominant relative contribution of a certain lamp type (marked grey) simultaneously demonstrated a high correlation with this lamp type. Overall, HPS lamps were the most widespread in Haifa in 2015 (with an average relative contribution of 32.8%), followed by MH lamps (22.0%), while LED lamps were considerably less frequent (15.6%).

Table 1 reports the performance of three alternative statistical models (linear regression, neural network, and random forest) developed to explain the variance of each lamp type relative contribution, under various sets of predictors, for the training and the testing sets

(see Section 2.4). As can be seen from the table, the performance is higher for the models with G/R and B/G ratios as predictors, compared to those with R, G, and B bands *per se*. We suppose that color ratios work better for predicting the relative contribution of a *certain lamp type* since it has a *certain spectral signature*. That is, the lamp of a certain type might be brighter or darker, and thus its aggregated R, G, and B levels per se will differ, but the ratios between those bands will remain the same. Indeed, in the considered set of observations, the variability of R, G, and B levels per se is much higher than the variability of their ratios (coefficients of variation for RGB channels are 0.72, 0.75, and 0.90, respectively, while for G/R and B/G ratios the corresponding numbers are 0.31 and 0.35). For all dependent variables and all predictor sets, random forest models perform generally better than either linear regression or neural network models. For three lamp types (HPS, MH, and MV), random forest models containing G/R and B/G ratios as predictors demonstrate high performance both for the training and the testing sets: $R^2 > 0.43$ (see Table 1, predictor sets 2nd–4th).

Table 1. The performance of models (in terms of R^2) with alternative predictor sets, for the training and the testing sets (dependent variable = relative contribution of a certain lamp type).

Model Type	Subset	Lamp Type						
		HPS	**MH**	**LED**	**CFL**	**LPS**	**Incand**	**MV**
Predictor set 1: R, G, B								
Linear regression	Training	0.34	0.23	0.03	0.06	0.16	0.09	0.17
	Testing	0.28	0.18	−0.11	0.00	0.07	0.03	0.13
Neural network	Training	0.39	0.07	−0.44	−0.32	−0.96	−0.32	−0.58
	Testing	0.34	−0.09	−1.27	−0.46	−1.72	−0.48	−0.96
Random forest	Training	0.88	0.86	0.77	0.75	0.79	0.81	0.82
	Testing	0.46	0.40	−0.17	0.19	0.00	0.25	0.39
Predictor set 2: G/R, B/G, GG/RB								
Linear regression	Training	0.52	0.33	0.02	0.11	0.21	0.09	0.22
	Testing	0.50	0.29	−0.08	0.06	0.08	0.00	0.17
Neural network	Training	0.53	0.39	0.04	0.14	0.19	0.17	0.31
	Testing	0.47	0.32	−0.12	0.04	−0.02	0.02	0.21
Random forest	Training	0.87	0.84	0.74	0.72	0.80	0.68	0.83
	Testing	0.55	0.47	−0.03	0.12	0.22	−0.16	0.53
Predictor set 3: G/R, B/G, Mahalanobis distance								
Linear regression	Training	0.53	0.35	0.03	0.11	0.21	0.10	0.34
	Testing	0.50	0.30	−0.08	0.07	0.10	−0.04	0.30
Neural network	Training	0.24	0.40	0.05	0.13	0.13	0.13	0.27
	Testing	0.19	0.32	−0.16	0.01	−0.04	−0.05	0.20
Random forest	Training	0.87	0.85	0.74	0.75	0.78	0.81	0.84
	Testing	0.53	0.47	0.13	0.20	0.19	0.38	0.43
Predictor set 4: G/R, B/G, Euclidean distance to the line								
Linear regression	Training	0.52	0.34	0.05	0.11	0.21	0.11	0.29
	Testing	0.50	0.29	−0.07	0.07	0.10	−0.12	0.24
Neural network	Training	0.26	0.36	0.06	0.11	0.13	0.13	0.29
	Testing	0.22	0.28	−0.25	−0.03	−0.04	−0.10	0.22
Random forest	Training	0.86	0.84	0.73	0.75	0.78	0.81	0.85
	Testing	0.49	0.45	0.06	0.19	0.19	0.38	0.53

Note: The lamps are sorted from left to right in descending order of their relative contributions (see results of unmixing analysis, reported in Appendix A Table A1).

Since models with the predictor sets 2nd–4th demonstrate similar performance, and proceeding from consideration of calculation simplicity, we run random forest models, built upon the whole set of observations, with G/R, B/G, and GG/RB ratios as predictors upon all pixels of the calibrated ISS image (see Figure 1b). Figure 7 reports resulting maps for two of the most frequent lamp types (HPS and MH) prevalent in Haifa. As can be seen from the figure, relatively higher contribution of HPS lamps in the outdoor lighting in Haifa coincide with the spatial pattern of municipal roads (see Figure 7a), while the pattern for MH lamps is more local and site-specific (see Figure 7b). In some regions of interest, HPS and MH lamps contribute to the outdoor lighting reversely. For example, in the Haifa Bay area, the impact of HPS lamps is pronounced, while MH lamps are absent (see Figure 7c); in contrast, in the areas hosting Khof Shemen industrial zone and Haifa airport, MH lamps are widely used while HPS lamps are absent (see Figure 7d).

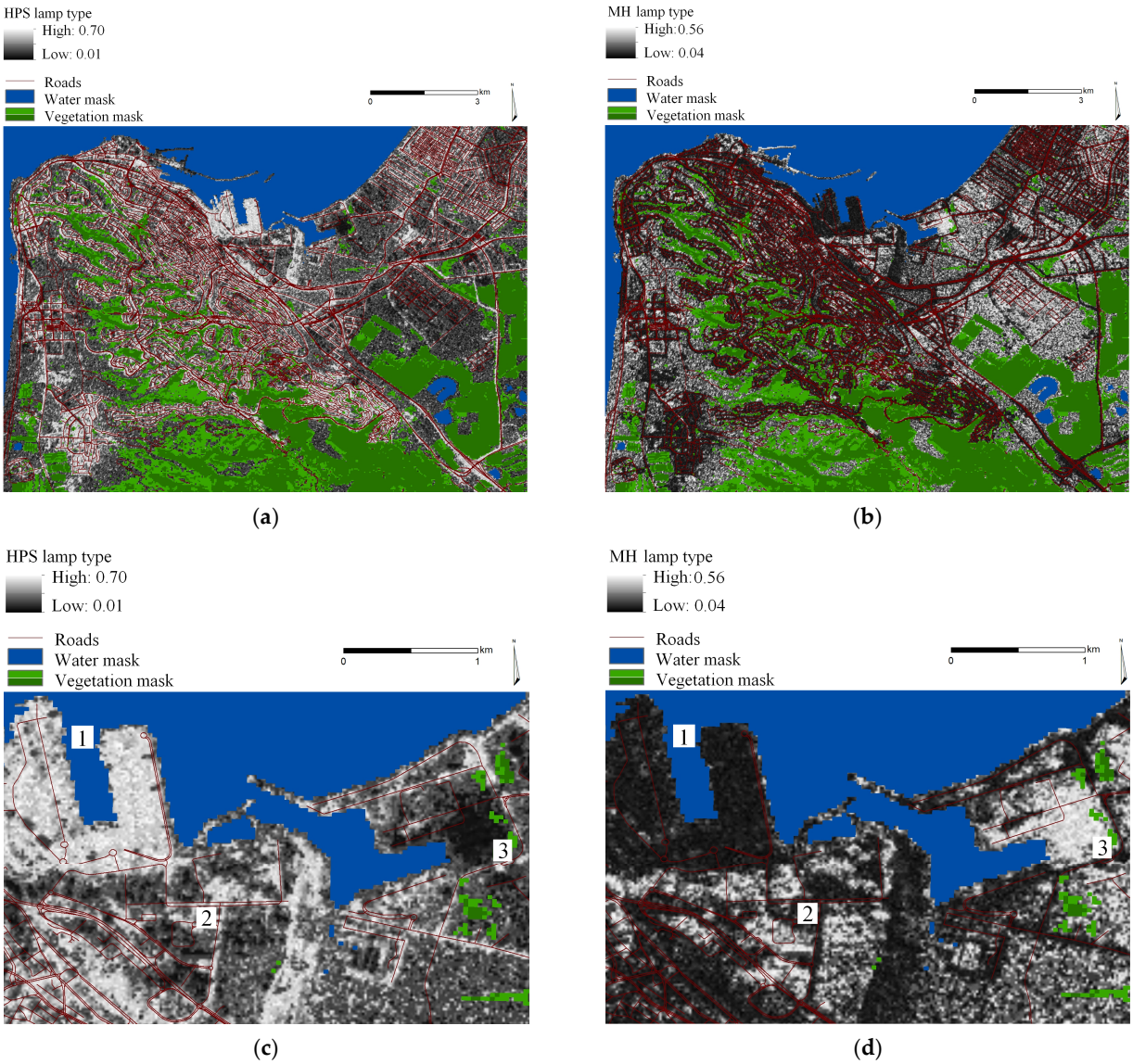


Figure 7. Model-anticipated relative contribution of High-Pressure Sodium (**a**,**c**) and Metal Halide (**b**,**d**) lamps in the outdoor lighting in Haifa area (**a**,**b**) and selected ROIs (**c**,**d**): "1" = Haifa Bay Area; "2" = Khof Shemen Industrial Zone; "3" = Haifa Airport. *Note*: Water and vegetation masks (marked, respectively, blue and green) were produced from Landsat 8 OLI/TIRS C2 L2 dataset image (path 174 row 037) acquired on 8 June 2015 [40]. For vegetation mask, normalized difference vegetation index (NDVI) was calculated as NDVI = (Band5 − Band6)/(Band5 + Band6) [41], and levels in 0.22–0.25 and >0.25 diapasons were marked as light and dark green. For the water mask, normalized difference moisture index (NDMI) was calculated as NDMI = (Band5 − Band4)/(Band5 + Band4) [42].

4. Discussion

In the present study, we tested for the possibility to identify on-ground lamp types from freely available satellite imagery of relatively coarse spatial and spectral resolution. To this end, we conducted a series of in situ NTL measurements in Haifa, Israel and combined these data with a radiometrically calibrated NTL image of the city taken from the ISS. Since the ISS image is of ~20-m resolution, each pixel likely represents light emission from a mixture of lamps. By applying unmixing analysis to the detailed spectral signatures of in situ NTL measurements, we estimated the relative contributions of different lamp types in each analyzed observation. Then, we tried to train statistical models to predict these relative contributions based exclusively on the ISS image, which represents RGB bands.

As our analysis indicates, contributions of two of the most widespread lamp types in the region, HPS and MH lamps, could be successfully predicted by random forest models. Using them, we restored HPS and MH lamps relative contribution to outdoor lighting of the whole Haifa area. The obtained HPS map demonstrated high concordance with the network of municipal roads (confirming the result obtained by Puschnig with co-authors for Vienna [29]), while the MH map showed notable coincidence with industrial facilities and the airport (see Figure 7).

In the developed models, we used three explanatory variables. Two of them, G/R and B/G ratios, are similar to those previously used by Sánchez de Miguel [28]. An additional informative predictor described a 'proximity' of the analyzed pixel of the ISS image to the lamp type in question. Interestingly, it turned out that lamps of the same type form clear-cut line segment-shaped loci in the G/R, B/G coordinate plane (see Figure 5). In this respect, we tried three alternative formalizations for the above-mentioned proximity: GG/RB ratio of the pixel, its Euclidean distance to the line, and its Mahalanobis distance to the locus. Without this additional explanatory variable, the models' performance was somewhat worse (with adjusted ΔR^2 up to -0.1, depending on the model type).

It should be mentioned that both Elvidge et al. [27] and Hale et al. [30] reached remarkably high classification accuracy (with errors of 4.7% and 7.5%, respectively), presumably due to either laboratory measurements [27] or high-resolution aerial imagery [30], incompatible with mixed pixels and used in the present analysis. However, their results cannot be directly compared with those presented here since we solved regression rather than classification problem, implying continuous rather than binary dependent variable. Yet, it seems reasonable to expect a better performance of our models if they were based on an image of better spectral (like in [27]) and/or spatial (like in [30]) resolution. Again, as mentioned above, we used the ISS image intentionally—given its free availability for many geographical sites. We think that our results argue for the principal possibility to assess the lamp type composition of outdoor lighting from the color satellite imagery.

Some limitations and perspectives of the study should be mentioned. First, proceeding from the available data, we did not succeed to obtain a reasonable spatial pattern for LED lamps' relative contribution in the outdoor lighting in Haifa. A trivial reason may be the insufficiency of the used data (small sample size, low prevalence of LEDs in the studied region in 2015). It also seems possible that the ISS imagery does not allow one to discriminate between LEDs due to their high spectral variability and, therefore, overlap with some other lamp types occurs (which becomes even more pronounced after considering the reflectance of the ground), such as MH lamps, in the B/G, G/R space [28]. It should be mentioned that Elvidge et al. [27] successfully discriminated between LED lamps from other types since they used almost non-overlapping red, green, blue, and NIR bands. Nowadays, LEDs' popularity is growing rapidly, mainly due to their versatility and energy-saving potential [27,28,43], and some precedents of total LED-based street lighting already exist [28,44]. At the same time, LEDs' primary emission peak, ~450–460 nm [27], radically distorts circadian rhythms and suppresses melatonin production in humans, contributing to sleep disorders [45], obesity [7], hormone-dependent cancers [9], and other diseases. Thus, further analysis is needed to explore the possibility to identify LED lamps from the ISS-provided imagery. It seems promising to exploit, in addition to ISS imagery,

VIIRS-provided panchromatic data, which covers also NIR diapason on night-time light. To obtain spatially upscaled panchromatic data, it seems rational first to teach some models (such as linear regressions, non-linear kernel regressions, random forest models, etc.) to associate between downscaled (to the resolution of ~742 m) ISS-provided RGB data and actual panchromatic data, and afterward to apply the best-performing model to predict panchromatic lights from the levels of actual RGB data (of ~20 m resolution). Alternatively, or in addition to, land-use data of fine spatial resolution, obtained from aerial imagery and LiDAR data (see for example [46–48]), might be used as an additional predictor for better discriminating between different lamp types. It is important to note that, given the good-performing models for *all lamp types*, a detailed spectrum might be easily restored for each pixel for the whole study area: for this sake, we should sum up the spectra of corresponding lamp types, weighted for their relative contributions. By this, we would be able to predict night-time hyperspectral information, which is currently not available from any of the existing satellites.

Second, the acquisition time of the used ISS-provided image and the in situ NTL measurements do not coincide perfectly, which may cause some inaccuracy in the herein obtained estimates. However, weather conditions in Israel are rather similar in March (when the in situ measurements were conducted) and in November (when the ISS image was taken): the average low-temperatures are ~11 °C in March and ~14 °C in November; the average sunshine is ~7 h for both months; and it is raining on average for 8.6 in March and 8 days in November [49]. Additionally, our sample did not include observations from residential areas, in which brightness may vary during the night [50]; instead, it included observations along major roads, entertainment areas, hospitals, and high-tech enterprises—that is, represented by streetlights of nearly-constant brightness during the night.

Finally, further testing of the proposed approach is required. For this sake, other ISS-provided images, which underwent radiometric calibration procedure [32,33], might be used. Given that cities might substantially differ in terms of building typologies and relationships between building heights and street widths [51], further research is needed to test the applicability of the obtained models to other geographical regions.

Author Contributions: Conceptualization, N.R., S.R. and A.B.; methodology, N.R., A.S.d.M. and A.B.; software, N.R. and A.S.d.M.; validation, N.R.; formal analysis, N.R.; investigation, N.R., S.R. and A.B.; resources, N.R.; data curation, N.R.; writing—original draft preparation, N.R.; writing—review and editing, A.S.d.M., S.R. and A.B.; visualization, N.R.; supervision, A.B.; project administration, N.R.; funding acquisition, N.R., S.R., A.S.d.M. and A.B. All authors have read and agreed to the published version of the manuscript.

Funding: This research was supported by the Council for Higher Education of Israel and by the Cities at Night Project.

Institutional Review Board Statement: Not applicable.

Informed Consent Statement: Not applicable.

Data Availability Statement: Data and the codes used in the analysis are available from the corresponding author upon request.

Acknowledgments: The authors thank three anonymous reviewers for highly valuable comments, which helped to improve the manuscript and make it more comprehensive to the reader.

Conflicts of Interest: The authors declare no conflict of interest. The funders had no role in the design of the study; in the collection, analyses, or interpretation of data; in the writing of the manuscript; or in the decision to publish the results.

Appendix A

Table A1. Unmixing results: The relative contribution of each lamp type into the detailed spectral signature of in situ observation (see text for explanation).

In Situ Obs. Number	Relative Contribution into In Situ Observation Detailed Spectral Signature of Standard Type Lamps							Max Correlation between Detailed Signatures of In Situ Obs. and Lamps	
	CFL	MH	HPS	LPS	Incand	MV	LED	Correlation	Lamp Type
504	0.085	0.659	0.067	0.060	0.014	0.000	0.114	0.720	LED
185	0.197	0.176	0.305	0.080	0.030	0.000	0.213	0.911	LED
566	0.022	0.058	0.201	0.044	0.568	0.009	0.097	0.957	Incand
467	0.000	0.024	0.772	0.054	0.000	0.000	0.150	0.945	HPS
238	0.194	0.072	0.323	0.000	0.008	0.307	0.095	0.634	MV
231	0.195	0.058	0.265	0.000	0.000	0.389	0.093	0.654	MV
97	0.000	0.065	0.664	0.169	0.000	0.000	0.101	0.937	HPS
465	0.000	0.024	0.760	0.103	0.000	0.000	0.113	0.930	HPS
286	0.083	0.465	0.336	0.000	0.000	0.000	0.116	0.747	LED
570	0.097	0.287	0.052	0.059	0.049	0.000	0.456	0.946	LED
112	0.040	0.305	0.372	0.243	0.013	0.000	0.026	0.806	HPS
565	0.000	0.019	0.151	0.027	0.638	0.002	0.164	0.979	Incand
431	0.000	0.056	0.671	0.151	0.036	0.000	0.087	0.889	HPS
466	0.000	0.024	0.755	0.100	0.000	0.000	0.121	0.932	HPS
433	0.000	0.085	0.629	0.119	0.000	0.000	0.166	0.913	LED
107	0.000	0.076	0.595	0.298	0.000	0.000	0.031	0.891	HPS
451	0.074	0.543	0.272	0.046	0.000	0.000	0.066	0.777	MH
1	0.247	0.098	0.161	0.000	0.000	0.386	0.108	0.670	MV
250	0.237	0.042	0.141	0.000	0.002	0.480	0.098	0.663	MV
432	0.000	0.068	0.608	0.075	0.062	0.000	0.187	0.936	LED
430	0.016	0.007	0.729	0.000	0.052	0.000	0.195	0.938	HPS
103	0.000	0.084	0.658	0.204	0.000	0.000	0.054	0.922	HPS
68	0.008	0.327	0.412	0.162	0.000	0.000	0.091	0.782	HPS
36	0.000	0.157	0.646	0.104	0.000	0.000	0.093	0.935	HPS
453	0.077	0.555	0.279	0.025	0.000	0.000	0.065	0.776	MH
168	0.025	0.358	0.478	0.045	0.000	0.000	0.094	0.849	HPS
40	0.000	0.058	0.674	0.176	0.000	0.000	0.092	0.935	HPS
64	0.021	0.345	0.411	0.148	0.000	0.000	0.074	0.741	HPS
440	0.007	0.184	0.584	0.107	0.000	0.000	0.118	0.898	HPS
452	0.078	0.551	0.269	0.041	0.000	0.000	0.062	0.775	MH
264	0.020	0.030	0.029	0.004	0.873	0.000	0.044	0.997	Incand
256	0.000	0.739	0.000	0.000	0.121	0.000	0.140	0.832	MH
261	0.392	0.152	0.235	0.045	0.026	0.000	0.149	0.843	LED
397	0.068	0.382	0.168	0.060	0.020	0.000	0.301	0.852	LED
109	0.000	0.081	0.586	0.311	0.000	0.000	0.023	0.885	HPS
445	0.036	0.511	0.294	0.116	0.008	0.000	0.035	0.803	MH
38	0.020	0.092	0.604	0.134	0.000	0.000	0.150	0.928	LED
450	0.076	0.570	0.266	0.010	0.000	0.000	0.079	0.762	MH
528	0.124	0.154	0.384	0.068	0.000	0.155	0.116	0.725	LED
104	0.000	0.086	0.614	0.268	0.000	0.000	0.032	0.900	HPS
559	0.516	0.036	0.161	0.000	0.000	0.203	0.085	0.789	CFL

Table A1. *Cont.*

In Situ Obs. Number	Relative Contribution into In Situ Observation Detailed Spectral Signature of Standard Type Lamps							Max Correlation between Detailed Signatures of In Situ Obs. and Lamps	
	CFL	MH	HPS	LPS	Incand	MV	LED	Correlation	Lamp Type
590	0.123	0.604	0.000	0.069	0.109	0.000	0.095	0.838	MH
29	0.114	0.090	0.525	0.094	0.002	0.000	0.174	0.930	LED
35	0.000	0.038	0.758	0.087	0.000	0.000	0.116	0.935	HPS
608	0.088	0.552	0.000	0.020	0.092	0.000	0.248	0.881	LED
187	0.004	0.123	0.574	0.151	0.008	0.000	0.140	0.927	HPS
31	0.055	0.060	0.640	0.152	0.000	0.000	0.093	0.926	HPS
129	0.000	0.052	0.693	0.181	0.000	0.000	0.074	0.931	HPS
508	0.409	0.409	0.044	0.000	0.000	0.025	0.112	0.714	CFL
260	0.034	0.675	0.149	0.086	0.000	0.000	0.057	0.752	MH
558	0.450	0.014	0.167	0.000	0.000	0.277	0.092	0.759	CFL
529	0.107	0.195	0.425	0.090	0.000	0.072	0.110	0.735	LED
556	0.532	0.038	0.153	0.000	0.000	0.198	0.079	0.797	CFL
564	0.000	0.045	0.239	0.060	0.455	0.000	0.202	0.934	Incand
518	0.013	0.027	0.103	0.045	0.049	0.000	0.762	0.983	LED
495	0.641	0.221	0.000	0.021	0.000	0.000	0.117	0.768	CFL
69	0.086	0.047	0.647	0.080	0.000	0.000	0.139	0.937	LED
429	0.000	0.045	0.688	0.000	0.070	0.000	0.197	0.930	HPS
101	0.000	0.071	0.643	0.179	0.000	0.000	0.106	0.934	HPS
291	0.093	0.263	0.296	0.000	0.005	0.155	0.189	0.725	LED
102	0.000	0.080	0.610	0.276	0.000	0.000	0.035	0.899	HPS
139	0.000	0.195	0.516	0.218	0.000	0.000	0.071	0.885	HPS
138	0.000	0.139	0.554	0.245	0.000	0.000	0.061	0.890	HPS
509	0.113	0.602	0.126	0.000	0.000	0.043	0.115	0.716	MH
100	0.000	0.086	0.547	0.367	0.000	0.000	0.000	0.841	HPS
607	0.053	0.554	0.000	0.000	0.111	0.000	0.282	0.887	LED
526	0.723	0.204	0.000	0.019	0.000	0.000	0.054	0.828	CFL
449	0.063	0.524	0.266	0.112	0.000	0.000	0.035	0.824	MH
517	0.038	0.184	0.492	0.219	0.000	0.000	0.067	0.840	HPS
520	0.002	0.000	0.004	0.000	0.057	0.018	0.919	0.984	LED
391	0.000	0.081	0.588	0.291	0.000	0.000	0.040	0.892	HPS
46	0.219	0.093	0.098	0.000	0.000	0.000	0.590	0.954	LED
523	0.016	0.133	0.439	0.373	0.000	0.000	0.040	0.766	HPS
519	0.028	0.002	0.009	0.000	0.060	0.021	0.880	0.984	LED
84	0.077	0.091	0.665	0.000	0.023	0.000	0.144	0.949	HPS
193	0.101	0.102	0.483	0.163	0.000	0.000	0.151	0.906	LED
589	0.032	0.645	0.000	0.000	0.179	0.000	0.144	0.810	MH
524	0.032	0.127	0.365	0.252	0.000	0.000	0.225	0.858	LED
591	0.474	0.419	0.000	0.018	0.025	0.000	0.064	0.747	CFL
563	0.000	0.039	0.154	0.073	0.630	0.000	0.103	0.971	Incand

Table A1. *Cont.*

In Situ Obs. Number	Relative Contribution into In Situ Observation Detailed Spectral Signature of Standard Type Lamps							Max Correlation between Detailed Signatures of In Situ Obs. and Lamps	
	CFL	MH	HPS	LPS	Incand	MV	LED	Correlation	Lamp Type
474	0.062	0.465	0.270	0.138	0.000	0.000	0.065	0.756	MH
16	0.028	0.013	0.189	0.021	0.028	0.019	0.701	0.977	LED
41	0.000	0.012	0.777	0.085	0.000	0.000	0.126	0.942	HPS
343	0.776	0.193	0.000	0.011	0.000	0.000	0.020	0.837	CFL
32	0.000	0.102	0.532	0.366	0.000	0.000	0.000	0.832	HPS
273	0.015	0.334	0.470	0.055	0.000	0.000	0.126	0.880	LED
208	0.005	0.108	0.344	0.150	0.032	0.000	0.361	0.965	LED
98	0.086	0.112	0.505	0.248	0.000	0.000	0.049	0.881	HPS
228	0.031	0.187	0.525	0.147	0.000	0.000	0.110	0.911	HPS
245	0.246	0.039	0.149	0.000	0.009	0.462	0.095	0.671	MV
446	0.023	0.537	0.293	0.126	0.000	0.000	0.021	0.820	MH
173	0.080	0.276	0.049	0.000	0.000	0.324	0.272	0.634	MH
605	0.082	0.548	0.000	0.017	0.091	0.000	0.262	0.893	LED
99	0.055	0.115	0.480	0.348	0.000	0.000	0.002	0.811	HPS
601	0.768	0.169	0.000	0.000	0.000	0.000	0.063	0.859	CFL
18	0.165	0.103	0.375	0.000	0.004	0.223	0.129	0.669	LED
555	0.609	0.069	0.123	0.000	0.000	0.126	0.073	0.818	CFL
530	0.473	0.079	0.080	0.030	0.000	0.062	0.275	0.772	LED
263	0.033	0.039	0.130	0.055	0.657	0.000	0.085	0.977	Incand
327	0.000	0.776	0.000	0.074	0.000	0.000	0.150	0.812	MH
600	0.767	0.165	0.000	0.000	0.000	0.000	0.068	0.856	CFL
557	0.305	0.015	0.191	0.000	0.000	0.403	0.087	0.678	MV
206	0.015	0.087	0.250	0.111	0.004	0.000	0.533	0.971	LED
562	0.000	0.058	0.201	0.106	0.527	0.000	0.108	0.936	Incand
265	0.024	0.015	0.038	0.013	0.895	0.002	0.012	0.999	Incand
372	0.093	0.076	0.160	0.039	0.525	0.000	0.106	0.957	Incand
604	0.032	0.525	0.000	0.000	0.115	0.000	0.328	0.916	LED
6	0.099	0.612	0.200	0.027	0.004	0.000	0.059	0.776	MH
606	0.047	0.558	0.000	0.000	0.114	0.000	0.282	0.885	LED
45	0.407	0.139	0.295	0.044	0.000	0.000	0.115	0.827	LED
266	0.052	0.031	0.032	0.010	0.843	0.000	0.032	0.998	Incand
39	0.000	0.052	0.673	0.179	0.000	0.000	0.096	0.935	HPS
15	0.019	0.014	0.089	0.013	0.037	0.022	0.805	0.976	LED
51	0.085	0.184	0.423	0.007	0.000	0.102	0.199	0.775	LED
583	0.094	0.573	0.217	0.000	0.000	0.000	0.115	0.729	MH
584	0.098	0.617	0.206	0.000	0.000	0.000	0.078	0.776	MH
42	0.002	0.197	0.620	0.060	0.000	0.000	0.121	0.893	HPS
292	0.052	0.193	0.317	0.000	0.000	0.283	0.155	0.604	MV
461	0.037	0.596	0.105	0.162	0.000	0.000	0.100	0.826	MH

Table A1. *Cont.*

In Situ Obs. Number	Relative Contribution into In Situ Observation Detailed Spectral Signature of Standard Type Lamps							Max Correlation between Detailed Signatures of In Situ Obs. and Lamps	
	CFL	MH	HPS	LPS	Incand	MV	LED	Correlation	Lamp Type
454	0.072	0.540	0.282	0.047	0.000	0.000	0.060	0.772	MH
439	0.011	0.081	0.619	0.146	0.001	0.000	0.141	0.917	HPS
471	0.057	0.469	0.271	0.141	0.000	0.000	0.062	0.772	MH
63	0.019	0.404	0.417	0.120	0.000	0.000	0.041	0.810	HPS
207	0.019	0.091	0.238	0.104	0.034	0.000	0.514	0.975	LED
468	0.000	0.031	0.743	0.091	0.000	0.000	0.136	0.933	HPS
585	0.151	0.436	0.187	0.000	0.000	0.078	0.148	0.652	CFL
599	0.757	0.165	0.000	0.000	0.000	0.000	0.078	0.853	CFL
197	0.114	0.138	0.415	0.210	0.000	0.000	0.123	0.887	LED
571	0.032	0.450	0.116	0.118	0.085	0.000	0.198	0.891	LED
434	0.000	0.080	0.687	0.131	0.000	0.000	0.101	0.928	HPS
448	0.063	0.501	0.275	0.128	0.000	0.000	0.034	0.807	MH
90	0.163	0.154	0.441	0.044	0.000	0.000	0.198	0.904	LED
399	0.060	0.308	0.158	0.060	0.116	0.006	0.292	0.899	LED
66	0.297	0.190	0.248	0.077	0.000	0.000	0.188	0.810	LED
375	0.043	0.249	0.466	0.100	0.000	0.000	0.142	0.926	LED
105	0.000	0.071	0.673	0.141	0.000	0.000	0.115	0.933	HPS
309	0.003	0.243	0.583	0.049	0.000	0.000	0.122	0.913	HPS
349	0.392	0.181	0.110	0.000	0.001	0.000	0.315	0.815	LED
198	0.010	0.119	0.535	0.310	0.000	0.000	0.026	0.867	HPS
475	0.055	0.488	0.255	0.142	0.000	0.000	0.060	0.780	MH
267	0.027	0.027	0.029	0.010	0.872	0.000	0.035	0.998	Incand
7	0.195	0.493	0.088	0.000	0.029	0.068	0.126	0.677	LED
227	0.006	0.128	0.606	0.159	0.000	0.000	0.101	0.919	HPS
199	0.003	0.111	0.549	0.312	0.000	0.000	0.025	0.871	HPS
262	0.679	0.175	0.021	0.029	0.000	0.000	0.096	0.791	CFL
244	0.239	0.042	0.147	0.000	0.048	0.432	0.093	0.672	MV
189	0.099	0.041	0.627	0.042	0.000	0.000	0.191	0.922	LED
5	0.041	0.569	0.274	0.084	0.000	0.000	0.032	0.817	MH
52	0.125	0.229	0.276	0.055	0.000	0.099	0.217	0.832	LED
376	0.060	0.251	0.449	0.097	0.000	0.000	0.142	0.930	LED
545	0.024	0.139	0.523	0.297	0.000	0.000	0.018	0.829	HPS
527	0.170	0.167	0.400	0.132	0.000	0.000	0.131	0.839	LED
405	0.063	0.541	0.162	0.131	0.000	0.000	0.102	0.774	MH
351	0.127	0.065	0.656	0.004	0.000	0.000	0.147	0.941	HPS
44	0.014	0.109	0.643	0.006	0.000	0.049	0.178	0.886	HPS
126	0.000	0.047	0.722	0.103	0.000	0.000	0.128	0.940	HPS
209	0.153	0.115	0.436	0.195	0.000	0.000	0.100	0.884	LED
398	0.061	0.321	0.159	0.057	0.079	0.000	0.323	0.890	LED

Table A1. *Cont.*

In Situ Obs. Number	Relative Contribution into In Situ Observation Detailed Spectral Signature of Standard Type Lamps							Max Correlation between Detailed Signatures of In Situ Obs. and Lamps	
	CFL	MH	HPS	LPS	Incand	MV	LED	Correlation	Lamp Type
350	0.581	0.189	0.138	0.000	0.000	0.000	0.092	0.770	CFL
462	0.041	0.610	0.107	0.143	0.000	0.000	0.099	0.828	MH
241	0.230	0.039	0.151	0.000	0.000	0.484	0.096	0.671	MV
521	0.023	0.007	0.028	0.004	0.054	0.032	0.851	0.985	LED
404	0.054	0.572	0.128	0.146	0.000	0.000	0.100	0.816	MH
569	0.238	0.063	0.000	0.000	0.000	0.000	0.699	0.950	LED
352	0.052	0.058	0.148	0.000	0.005	0.000	0.737	0.976	LED
2	0.216	0.296	0.061	0.000	0.000	0.242	0.185	0.648	CFL
284	0.083	0.531	0.262	0.000	0.000	0.000	0.124	0.719	MH
447	0.035	0.515	0.283	0.131	0.011	0.000	0.025	0.802	MH
498	0.586	0.257	0.000	0.000	0.000	0.000	0.157	0.760	CFL
108	0.000	0.058	0.642	0.141	0.000	0.000	0.159	0.928	LED
196	0.064	0.098	0.577	0.132	0.000	0.000	0.129	0.925	HPS
540	0.183	0.027	0.138	0.000	0.021	0.399	0.232	0.697	LED
95	0.068	0.077	0.679	0.006	0.000	0.000	0.170	0.940	HPS
85	0.016	0.135	0.611	0.054	0.010	0.000	0.175	0.938	LED
141	0.000	0.288	0.462	0.126	0.000	0.000	0.124	0.877	HPS
113	0.041	0.482	0.234	0.189	0.025	0.000	0.028	0.838	MH
307	0.020	0.396	0.381	0.091	0.037	0.000	0.075	0.861	LED
37	0.186	0.106	0.458	0.146	0.000	0.000	0.104	0.733	LED
477	0.133	0.025	0.193	0.000	0.000	0.555	0.095	0.689	MV
476	0.133	0.026	0.200	0.000	0.000	0.549	0.091	0.686	MV
13	0.147	0.444	0.152	0.174	0.047	0.000	0.037	0.886	MH
143	0.036	0.091	0.600	0.233	0.000	0.000	0.040	0.878	HPS
542	0.181	0.027	0.139	0.000	0.033	0.391	0.230	0.701	LED
437	0.000	0.105	0.601	0.218	0.000	0.000	0.077	0.879	HPS
28	0.002	0.079	0.641	0.165	0.000	0.000	0.113	0.928	HPS
578	0.117	0.549	0.049	0.010	0.072	0.000	0.203	0.850	LED
580	0.092	0.583	0.162	0.000	0.022	0.000	0.143	0.806	LED
582	0.111	0.549	0.178	0.000	0.000	0.018	0.145	0.684	MH
541	0.174	0.029	0.127	0.000	0.035	0.371	0.264	0.755	LED
200	0.000	0.114	0.607	0.169	0.000	0.000	0.109	0.922	HPS
412	0.000	0.537	0.155	0.097	0.059	0.000	0.152	0.728	LED
268	0.006	0.016	0.261	0.000	0.008	0.000	0.710	0.990	LED
435	0.000	0.081	0.606	0.208	0.026	0.000	0.080	0.873	HPS
218	0.051	0.354	0.333	0.121	0.015	0.000	0.126	0.893	LED
561	0.000	0.103	0.373	0.200	0.230	0.000	0.095	0.826	LED
534	0.100	0.109	0.457	0.217	0.000	0.063	0.055	0.795	HPS
Avg.	**0.111**	**0.220**	**0.328**	**0.088**	**0.052**	**0.044**	**0.156**		

References

1. Tsao, J.Y.; Waide, P. The world's appetite for light: Empirical data and trends spanning three centuries and six continents. *LEUKOS-J. Illum. Eng. Soc. N. Am.* **2010**, *6*, 259–281. [CrossRef]
2. Kyba, C.C.M.; Kuester, T.; De Miguel, A.S.; Baugh, K.; Jechow, A.; Hölker, F.; Bennie, J.; Elvidge, C.D.; Gaston, K.J.; Guanter, L. Artificially lit surface of Earth at night increasing in radiance and extent. *Sci. Adv.* **2017**, *3*, e1701528. [CrossRef]
3. Falchi, F.; Cinzano, P.; Duriscoe, D.; Kyba, C.C.M.; Elvidge, C.D.; Baugh, K.; Portnov, B.A.; Rybnikova, N.A.; Furgoni, R. The new world atlas of artificial night sky brightness. *Sci. Adv.* **2016**, *2*, e1600377. [CrossRef]
4. Falchi, F.; Furgoni, R.; Gallaway, T.A.A.; Rybnikova, N.A.A.; Portnov, B.A.A.; Baugh, K.; Cinzano, P.; Elvidge, C.D.D. Light pollution in USA and Europe: The good, the bad and the ugly. *J. Environ. Manag.* **2019**, *248*, 109227. [CrossRef]
5. Balsa-Barreiro, J.; Li, Y.; Morales, A.; Pentland, A. "Sandy" Globalization and the shifting centers of gravity of world's human dynamics: Implications for sustainability. *J. Clean. Prod.* **2019**, *239*, 117923. [CrossRef]
6. Kloog, I.; Haim, A.; Stevens, R.G.; Portnov, B.A. Global co-distribution of light at night (LAN) and cancers of prostate, colon, and lung in men. *Chronobiol. Int.* **2009**, *26*, 108–125. [CrossRef]
7. McFadden, E.; Jones, M.E.; Schoemaker, M.J.; Ashworth, A.; Swerdlow, A.J. The relationship between obesity and exposure to light at night: Cross-sectional analyses of over 100,000 women in the Breakthrough Generations Study. *Am. J. Epidemiol.* **2014**, *180*, 245–250. [CrossRef]
8. Garcia-Saenz, A.; Sánchez de Miguel, A.; Espinosa, A.; Valentin, A.; Aragonés, N.; Llorca, J.; Amiano, P.; Martín Sánchez, V.; Guevara, M.; Capelo, R.; et al. Evaluating the Association between Artificial Light-at-Night Exposure and Breast and Prostate Cancer Risk in Spain (MCC-Spain Study). *Environ. Health Perspect.* **2018**, *126*, 047011. [CrossRef]
9. Haim, A.; Portnov, B.A. *Light Pollution as a New Risk Factor for Human Breast and Prostate Cancers*; Springer: Dordrecht, The Netherlands, 2013; ISBN 9789400762206.
10. Longcore, T.; Rich, C. Ecological light pollution. *Front. Ecol. Environ.* **2004**, *2*, 191–198. [CrossRef]
11. Hölker, F.; Wolter, C.; Perkin, E.K.; Tockner, K. Light pollution as a biodiversity threat. *Trends Ecol. Evol.* **2010**, *25*, 681–682. [CrossRef]
12. Gaston, K.J.; Bennie, J.; Davies, T.W.; Hopkins, J. The ecological impacts of nighttime light pollution: A mechanistic appraisal. *Biol. Rev.* **2013**, *88*, 912–927. [CrossRef]
13. Owens, A.C.S.; Cochard, P.; Durrant, J.; Farnworth, B.; Perkin, E.K.; Seymoure, B. Light pollution is a driver of insect declines. *Biol. Conserv.* **2020**, *241*, 108259. [CrossRef]
14. Lyytimäki, J. Towards eco-efficient and enjoyable lighting. *Br. GSDR* **2015**.
15. Riegel, K.W. Light pollution. *Science* **1973**, *179*, 1285–1291. [CrossRef]
16. Zhang, Q.; Wang, P.; Chen, H.; Huang, Q.; Jiang, H.; Zhang, Z.; Zhang, Y.; Luo, X.; Sun, S. A novel method for urban area extraction from VIIRS DNB and MODIS NDVI data: A case study of Chinese cities. *Int. J. Remote Sens.* **2017**, *38*, 6094–6109. [CrossRef]
17. Kyba, C.C.M. Is light pollution getting better or worse? *Nat. Astron.* **2018**, *2*, 267–269. [CrossRef]
18. Falchi, F.; Bará, S. A linear systems approach to protect the night sky: Implications for current and future regulations. *R. Soc. Open Sci.* **2020**, *7*, 201501. [CrossRef]
19. Morgan-Taylor, M. *Regulating Light Pollution in Europe: Legal Challenges and Ways Forward*; Routledge: New York, NY, USA, 2015.
20. Cho, S.; Lee, M.; Choi, H.; Korean, H.K.-J. Calculation and Regulation Proposal of Light Pollution from Road Lightings. *J. Korean Inst. Illum. Electr. Install. Eng.* **2011**, *25*, 21–26. [CrossRef]
21. Gaston, K.; Duffy, J.; Gaston, S.; Bennie, J.; Oecologia, T.D. Human alteration of natural light cycles: Causes and ecological consequences. *Oecologia* **2014**, *176*, 917–931. [CrossRef]
22. Schroer, S.; Hölker, F. *Impact of Lighting on Flora and Fauna*; Springer: Berlin, Germany, 2016. [CrossRef]
23. Lockley, S.; Brainard, G.C.; Czeisler, C.A. High sensitivity of the human circadian melatonin rhythm to resetting by short wavelength light. *J. Clin. Endocrinol. Metab.* **2003**, *88*, 4502–4505. [CrossRef]
24. Hatori, M.; Gronfier, C.; Van Gelder, R.N.; Bernstein, P.S.; Carreras, J.; Panda, S.; Marks, F.; Sliney, D.; Hirota, T.; Furukawa, T.; et al. Global rise of potential health hazards caused by blue light-induced circadian disruption in modern aging societies. *Npj Aging Mech. Dis.* **2017**, *3*, 9. [CrossRef]
25. Wiltschko, W.; Munro, U.; Ford, H.; Wiltschko, R. Red light disrupts magnetic orientation of migratory birds. *Nature* **1993**, *364*, 525–527. [CrossRef]
26. Tapia Ayuga, C.; Sánchez de Miguel, A.; Zamorano Calvo, J. LICA-UCM lamps spectral database. *Ene* **2017**, *8*, 29.
27. Elvidge, C.D.; Keith, D.M.; Tuttle, B.T.; Baugh, K.E. Spectral identification of lighting type and character. *Sensors* **2010**, *10*, 3961–3988. [CrossRef] [PubMed]
28. Sánchez de Miguel, A.; Kyba, C.C.M.; Aubé, M.; Zamorano, J.; Cardiel, N.; Tapia, C.; Bennie, J.; Gaston, K.J. Colour remote sensing of the impact of artificial light at night (I): The potential of the International Space Station and other DSLR-based platforms. *Remote Sens. Environ.* **2019**, *224*, 92–103. [CrossRef]
29. Puschnig, J.; Posch, T.; Uttenthaler, S. Night sky photometry and spectroscopy performed at the Vienna University Observatory. *J. Quant. Spectrosc. Radiat. Transf.* **2014**, *139*, 64–75. [CrossRef]

30. Hale, J.D.; Davies, G.; Fairbrass, A.J.; Matthews, T.J.; Rogers, C.D.F.; Sadler, J.P. Mapping Lightscapes: Spatial Patterning of Artificial Lighting in an Urban Landscape. *PLoS ONE* **2013**, *8*, e61460. [CrossRef] [PubMed]
31. Search Photos. Available online: https://eol.jsc.nasa.gov/SearchPhotos/ (accessed on 7 April 2020).
32. Home-Savestars Consulting S.L. Available online: http://www.savestarsconsulting.com/en/index/ (accessed on 6 May 2021).
33. Sánchez de Miguel, A. Colour remote sensing of the impact of artificial light at night (II): Calibration of DSLR-based images from the International Space Station. *Remote. Sens. Environ.* **2021**, *264*, 112611. [CrossRef]
34. Illuminance Spectrophotometer CL-500A. Available online: https://www.konicaminolta.com/instruments/download/catalog/light/pdf/cl500a_catalog_eng.pdf (accessed on 6 May 2021).
35. MODTRAN®. Available online: http://modtran.spectral.com/ (accessed on 13 June 2021).
36. Shi, C.; Wang, L. Incorporating spatial information in spectral unmixing: A review. *Remote Sens. Environ.* **2014**, *149*, 70–87. [CrossRef]
37. Bro, R.; De Jong, S. A fast non-negativity-constrained least squares algorithm. *J. Chemom.* **1997**, *11*, 393–401. [CrossRef]
38. Mahalanobis, P. On the generalized distance in statistics. 1936.
39. Breiman, L. Random forests. *Mach. Learn.* **2001**, *45*, 5–32. [CrossRef]
40. EarthExplorer. Available online: https://earthexplorer.usgs.gov/ (accessed on 22 June 2021).
41. Landsat Normalized Difference Vegetation Index. Available online: https://www.usgs.gov/core-science-systems/nli/landsat/landsat-normalized-difference-vegetation-index?qt-science_support_page_related_con=0#qt-science_support_page_related_con (accessed on 22 June 2021).
42. Normalized Difference Moisture Index. Available online: https://www.usgs.gov/core-science-systems/nli/landsat/normalized-difference-moisture-index (accessed on 22 June 2021).
43. Schubert, E.F.; Kim, J.K. Solid-state light sources getting smart. *Science* **2005**, *308*, 1274–1278. [CrossRef]
44. Kyba, C.C.M.; Ruby, A.; Kuechly, H.U.; Kinzey, B.; Miller, N.; Sanders, J.; Barentine, J.; Kleinodt, R.; Espey, B. Direct measurement of the contribution of street lighting to satellite observations of nighttime light emissions from urban areas. *Light. Res. Technol.* **2020**. [CrossRef]
45. Czeisler, C.A. Perspective: Casting light on sleep deficiency. *Nature* **2013**, *497*, S13. [CrossRef] [PubMed]
46. Buján, S.; González-Ferreiro, E.; Reyes-Bueno, F.; Barreiro-Fernández, L.; Crecente, R.; Miranda, D. Land Use Classification from Lidar Data and Ortho-Images in a Rural Area. *Photogramm. Rec.* **2012**, *27*, 401–422. [CrossRef]
47. Hermosilla, T.; Ruiz, L.; Recio, J.; Balsa-Barreiro, J. Land-Use Mapping of Valencia City Area from Aerial Images and LiDAR Data. In Proceedings of the GEOProcessing 2012: The Fourth International Conference in Advanced Geographic Information Systems, Applications and Services, Valencia, Spain, 30 January–4 February 2012; pp. 232–237.
48. Megahed, Y.; Shaker, A.; Sensing, W.Y.-R. Fusion of Airborne LiDAR Point Clouds and Aerial Images for Heterogeneous Land-Use Urban Mapping. *Remote Sens.* **2021**, *13*, 814. [CrossRef]
49. Haifa, Israel-Detailed Climate Information and Monthly Weather Forecast | Weather Atlas. Available online: https://www.weather-atlas.com/en/israel/haifa-climate#climate_text_4 (accessed on 26 October 2021).
50. Bará, S.; Rodríguez-Arós; Pérez, M.; Tosar, B.; Lima, R.C.; Sánchez de Miguel, A.; Zamorano, J. Estimating the relative contribution of streetlights, vehicles, and residential lighting to the urban night sky brightness. *Light. Res. Technol.* **2019**, *51*, 1092–1107. [CrossRef]
51. Hermosilla, T.; Palomar-Vázquez, J.; Balaguer-Beser, Á.; Balsa-Barreiro, J.; Ruiz, L.A. Using street based metrics to characterize urban typologies. *Comput. Environ. Urban Syst.* **2014**, *44*, 68–79. [CrossRef]